Bearingless Induction Motor Design with the DPNV Winding and Reduced Axial Length Pole-Specific Rotor

Jiahao Chen and Eric L Severson

Department of Electrical and Computer Engineering, University of Wisconsin-Madison, WI, USA
horychen@zju.edu.cn, eric.severson@wisc.edu

Abstract

This paper investigates the design of bearingless induction motor that uses a dual purpose no voltage (DPNV) winding and pole-specific rotor. The investigation is motivated by a previous study that showed that by integrating these two technologies into a bearingless induction motor, a high performance machine can be created for industrial compressor applications (over 95% efficiency, over 15 kNm/m^3 torque density, and less than 2.5% current for supporting the rotor weight). The use of parallel pole-specific rotor significantly reduces the rotor axial length, improving rotor dynamics. However, implementing the DPNV winding is difficult because it results in an asymmetric winding for two preferred pole combinations of the induction machine. This paper investigates these asymmetries and the challenges that they pose for the bearingless machine performance.

Complex winding factors are introduced as a tool to explore the physics behind each design in terms of sub-harmonics and winding asymmetry. Transient FEA is used to obtain steady state suspension force vectors as a function of suspension current phase angle for five selected optimal designs. The results are visualized as polar plot, where relevant performance measures are proposed. It is found that a symmetric winding (with or without sub-harmonics) has a circular force trajectory, while asymmetric winding causes an undesired elliptical force trajectory that degrades the machines force rating. Moreover, it is found that asymmetric sub-harmonics alone can also lead to this elliptical force trajectory. It is revealed by further studying the force error angle trajectory that the force error angle is generally a function of suspension current phase angle, which has implications for the optimization of these machines. In conclusion, this paper shows that the asymmetric DPNV winding can result in a high performance design, which enables higher performance pole combinations for bearingless induction motors.

Keywords: dual purpose no voltage winding, magnetic levitation, asymmetry, sub-harmonics.

Nomenclature

$p,\ p_s$	the pole pair number of torque field and suspension field, respectively.
$Q_r,\ Q'_r$	the total rotor slot number, and the cage slot number of parallel pole-specific rotor.
$h,\ v$	absolute harmonic order, and relative harmonic order.

1 Introduction

Induction motors are widely used in both commercial and industrial applications, including compressors, blowers, spindles, speed servo motors, and traction motors. The bearingless version of the induction motor technologies have been developed since the early 1990s [1, ch. 13]. Innovation in the design of this machine can be divided into the following three paths: geometry optimization, stator winding, and rotor winding. These three innovation pathways are now briefly reviewed, with emphasis placed on the stator and rotor winding approach. This paper's goal is to explore how promising innovations in the stator and rotor winding can be combined to form a practical bearingless machine and identify areas where further research is needed.

The geometry optimization of a bearingless induction motor is more complicated than synchronous machines due to rotor currents. A study presented in [2] develops techniques to optimize the machine design, including computationally-efficient modeling techniques to rapidly reach steady state and an algorithm to estimate the machine's breakdown slip.

The stator winding for a bearingless motor is responsible for creating two magnetic fields, one field for motor operation (p pole-pairs) and a second field for controlling suspension forces (p_s pole-pairs, where $p_s = p \pm 1$). Winding approaches can be broadly classified as either "separated" or "combined." *Separated windings* are actually two independent stator windings that share the same stator slots; one winding creates p pole-pairs and the second winding creates p_s pole-pairs [1]. In magnetic levitation systems, the suspension winding is typically overdimensioned (more ampere-turn capacity is allocated than required) to build in a safety factor for the suspending the motor shaft. Typical bearingless motors with separated windings allocate 30–50% of the slot space to the levitation winding, which derates the machine's torque density by 30–50% [3]. In previous work, the authors have found that most machines actually require only $< 2.5\%$ of slot current to support the rotor's weight [3]. This means that during normal operation, the slot space that has been allocated to the suspension winding is underutilized.

As an alternate to separated windings, *combined windings* are winding approaches that use the same stator coils for both torque and force creation. This allows the stator current capacity to be used more effectively because the slot current can be dynamically allocated between creating torque and force. In a motor system where the nominal load is gravity and other force disturbance events are rare (i.e., compressor surge or passing through a critical speed), a combined winding approach can enable a significant improvement in machine performance and power density. There are several combined winding approaches that have been proposed in the literature. These include multi-phase [4, 5], dual purpose no voltage ("DPNV") [6, 7], multi-sector [8, 9], and middle-point current injection windings [10]. Of these, multi-phase and DPNV combined windings offer the highest potential for performance, because they allow independent motor d and q current control.

It was shown in [11] that the DPNV winding is a circuit-based implementation of the multi-phase winding. From a machine perspective, the two windings are identical. However, the DPNV winding has the advantage of enabling the motor operation to be controlled with a conventional three phase motor drive that has no knowledge of the machine being bearingless. For significant power and critical industrial applications, using a conventional motor drive (with no knowledge of the suspension operation) is very attractive. A machine owner can purchase a well-established and trusted commercial product for the critical power path and a specialized drive for the low power suspension operation. For this reason, the authors of this paper believe that the DPNV winding is a promising technology for the commercialization of industrial-scale bearingless motors.

Early bearingless induction motors utilized squirrel cage rotors [12, 13]. Under nominal loading, the bearingless machine's suspension field rotates at a different speed than the rotor. This induces current in squirrel cage rotor circuit which has been found to be problematic [1, p.255]. The squirrel cage leads to inevitable delay in regulation of suspension force [14], and results in inefficient magnetic levitation, because excessive stator current is needed to create the suspension magnetic field, as the suspension slip frequency gets large at high speeds [15].

Alternative rotor winding approaches have since been developed that are designed to prevent current from being induced in the rotor. For example, the highest power bearingless induction motor reported in literature is tested at 30 kW using a wound-rotor [16]. The wound-rotor induction motor has been historically proposed for soft starting [17]. If the wound-rotor winding is designed such that it has zero winding factor for the p_s pole-pair suspension field, it will not

link the suspension field and therefore no current will be induced [18]. This makes the rotor structure an effective alternative to the squirrel cage rotor.

This same principle (of not linking the suspension flux) has been applied to the design of cage rotors. In [19], a "pole-specific" (PS) cage rotor is proposed that consists of multiple isolated cages, each with four bars connected in series in a manner that prevents them from linking a two pole suspension field (for a bearingless machine with $p=2, p_s=p-1$). This structure was later optimized in [20] to reduce rotor resistance. A similar structure has been developed for machines with four pole suspension fields (bearingless machine with $p=1, p_s=p+1$), where each isolated rotor cage consists of two bars placed on opposite sides of the rotor [1, 21]. These two cage rotor designs will be referred to as the "isolated PS rotor" in this paper. While the isolated PS rotor offers a high performance solution from an electric perspective, it poses mechanical challenges. Isolated end-plates must be located at each end of the rotor which adds significant axial length. Recently, a new cage rotor structure has been developed by *Chen et. al.* in [22] to reduce the number of end-plates (and therefore the axial length). This structure is referred to as a "parallel PS rotor" in this paper because it uses a common end ring to connect all rotor cages in parallel on one end of the rotor. *Chen et. al.* have generalized the concept and shown how the rotor can be designed for all pole-configurations with $p_s \geq 2$.

The authors of this paper propose developing a bearingless induction motor that utilizes both the parallel PS rotor (to improve electric performance and simplify the mechanical design) and the DPNV stator winding (to increase torque density and efficiency). Unfortunately, two potentially critical problems arise when trying to design a machine of this configuration for industrial applications. First, many DPNV windings that match the preferred slot-pole combinations of induction machines will create subharmonic airgap magnetic fields when excited with suspension currents. These fields will link the pole-specific rotor, inducing currents and potentially degrading performance. Second, these industrial-scale machines often prefer pole-combinations with either $p = 3$ or $p_s = 3$. Such machines will violate a symmetry condition of three phase DPNV windings, resulting in an asymmetric stator winding that may cause unacceptable force performance. This paper investigates DPNV windings with subharmonic fields and MMF asymmetry. The paper analyzes whether example practical machines which use these windings can still function as high performance bearingless motors and identifies areas where future research is needed to make these machines practical.

This paper will first summarize the parallel PS rotor design of [22] and explain the primary differences between isolated and parallel PS rotors in Section 2. Next, Section 3 summarizes the DPNV winding and presents the design of DPNV windings for induction machines that violate the symmetry condition. The asymmetries that result in these machine windings are explained and analyzed in Section 4 using complex winding factors. Inherent suspension sub-harmonics of the DPNV winding are investigated in Section 5. Finally, the influence of asymmetry and harmonics on the machine's suspension force performance is analyzed in Section 6.

2 Pole Specific Rotor with Reduced Axial Length

This section summarizes the parallel PS rotor design utilized in this paper (recently developed in [22]) and explains how it differs from the more established isolated PS rotor design of [19,21].

The parallel PS rotor circuit consists of a common end-ring on one axial end and multiple end-rings on the other end. Each cage has Q'_r rotor bars that are connected in parallel so that the spacing between the bars is a suspension pole-pair. Compared with the isolated PS rotor, this type of PS rotor has significantly less axial length because all end-connections at one end of the rotor are removed (apart from the common end-ring). Example isolated PS rotor

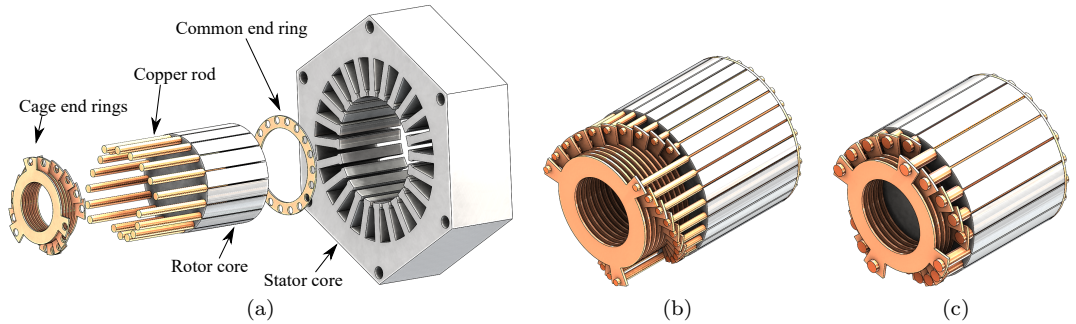

Figure 1: Parallel PS rotors with (a),(b) $Q'_r = p_s = 3$ and $Q_r = 18$, 30; (c) $Q'_r = p_s = 4$, $Q_r = 20$.

prototypes for $p = 1, p_s = 2$ can be found in [23, 24] and a prototype of the new parallel PS rotor ($Q'_r = p_s = 2$) is documented in [2, 22].

For $p = 1$ bearingless induction machines, the parallel PS rotor is recognizable as an isolated PS rotor where the axial end rings on one side have been replaced by a common end-ring. However, notable differences arise for $p \geq 2$. In $p = 2$ bearingless induction motors, if a $p_s = p - 1$ design is desired, the isolated PS rotor utilizes four series-connected rotor bars per cage [19] while the parallel PS rotor does not exist because only $Q'_r = p_s = 1$ rotor bar could be used in a cage; this design would be invalid as at least two bars are needed for rotor current to flow. Alternatively, a $p = 2$, $p_s = p + 1$ design can utilize a parallel PS rotor, but no isolated PS rotors have been documented with $p_s > 2$. In other words, if a $p = 2$ motor is desired, one can choose between a $p_s = 1$ isolated PS rotor and a $p_s = 3$ parallel PS rotor, and the latter usually has a shorter end connection region. Example CAD drawings of $Q'_r = p_s = 3$ parallel PS rotors are shown in Figure 1a with an exploded view and Figure 1b. Furthermore, the parallel PS rotor concept can be generalized for all $p \geq 3$ motors, and an example $Q'_r = p_s = 4$ parallel PS rotor for $p = 3, 5$ motor is sketched in Figure 1c.

This paper is particularly interested in developing high p_s design that can potentially reduce the rotor axial length of a bearingless induction motor. The rest of this section will summarize the key properties of the parallel PS rotor from [22].

2.1 Pole-Specific Rotor with Parallel Connected Bars

The fundamental premise of the parallel PS rotor is that a single cage is composed of bars which span a suspension pole-pair. Because the cage bars span a suspension pole-pair, they do not link the suspension field. Since a cage must consist of more than one bar, this rotor concept only works if the motor has at least 2 suspension pole-pairs, i.e. $p_s \geq 2$. The complete rotor consists of multiple cages. The cages share a common end-ring on one side of the rotor, but on the other side they have separate end-rings, as shown in the exploded view in Fig 1a.

2.2 Common End-ring

Using a common end-ring to replace the end-connections at one side of the rotor, results in 50% less end-connection space. This saves remarkable axial length for high speed applications where critical speeds limit the rotor axial length. *Chen et. al.* show in [22, Sec.II-B] that this design preserves the pole-specific property and has no performance penalty.

While the currently described parallel PS rotor does not work for $p = 2$, $p_s = 1$ machines, one can infer from this discussion that this can actually be accomplished by placing end-connections on both rotor ends as exemplified in Figure 2.

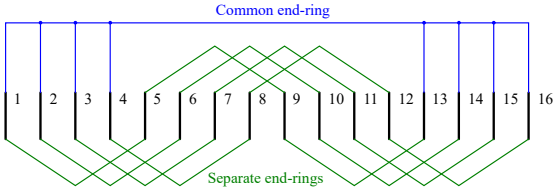

Figure 2: Common end-ring PS rotor design proposed for $Q_r = 16, p = 2, p_s = 1$.

2.3 Multiple Separate Cages

The idea of a parallel PS rotor is to not induce rotor current from the p_s pole-pair suspension field. To this end, the number of bars in a cage, denoted as Q'_r, depends on p_s. Specifically, Q'_r is determined by the fact that a cage with Q'_r bars does will not have rotor current induced by a magnetic field whose pole pair number p_s is multiple of Q'_r.

Using multiple cages, each with Q'_r bars results in a different bar spacing parameter $\alpha_c = \frac{2\pi}{Q'_r}$ from a traditional squirrel cage with Q_r bars. By analyzing the T-equivalent circuit of a parallel PS rotor, the rotor bar impedance is found to be a function of the number of cages N_c when Q_r is fixed, and the conclusion of [22] is that converting a squirrel cage rotor to a parallel PS rotor would result in comparable or even improved motor performance.

It is recommended to let one cage hold as many rotor bars as possible, as an effort to reduce rotor axial length. For instance, a parallel PS rotor with $p = 3,\ p_s = 4$ can reduce the number of end-rings by 75% as compared to a $p = 1,\ p_s = 2$ isolated PS rotor that has the same number of rotor slots, because the parallel PS rotor has one common end-ring and it groups $Q'_r = p_s = 4$ bars in a single cage.

2.4 Design rules

For a p pole-pair bearingless induction motor to be able to use the parallel PS rotor winding, it must satisfy the design rules listed in (1) according to [22]

$$p_s = p \pm 1, \quad p_s \geq 2, \tag{1a}$$

$$Q'_r = p_s/k \tag{1b}$$

where k can be any integer to make $Q'_r \geq 2$ an integer. Then, by deciding the number of cages, N_c, the total slot number is determined as $Q_r = N_c Q'_r$.

For most applications, the choice of k is recommended to be 1, such that Q'_r is maximized. For a certain Q_r value, this gives a minimal N_c as an effort to reduce rotor axial length. However, the choice of $k > 1$ allows for more values of Q_r to be usable, and such demand could emerge when a high p induction motor is desired.

3 Stator Winding Design for Induction Motors

This paper studies the DPNV winding as the combined winding approach for bearingless induction motors. The DPNV winding has been shown to have equivalent performance to multi-phase winding [11]. One major reason to use DPNV winding is that the DPNV winding allows to use any commercially available motor drive product for the maglev system, and the engineer would only need to build the suspension inverter part. However, the literature has been avoiding designing a $p = 3$ or $p_s = 3$ bearingless motors using DPNV winding (see, e.g., [25]). According to [26, Table III], the symmetry conditions state that for an m-phase motor, m and p must be co-prime and m and p_s must be co-prime. In other words, symmetric three phase DPNV winding cannot have $p = 3$ or $p_s = 3$.

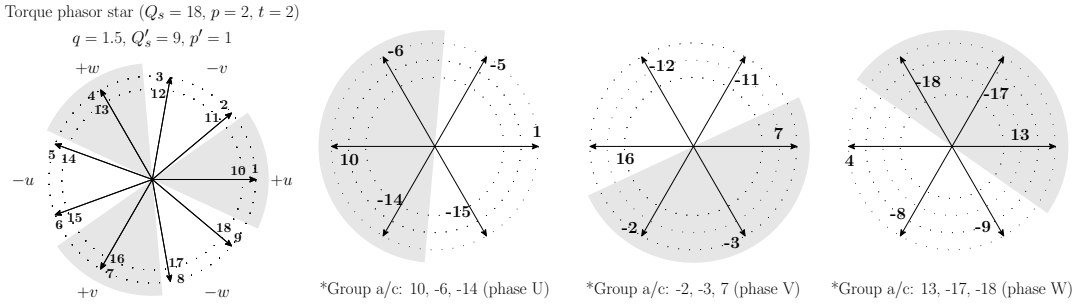

Figure 3: Star of slots plot for a winding with $Q_s = 18$, $p = 2$ $p_s = 3$, a) at torque frequency, b) at suspension frequency.

The most popular pole pair numbers for industrial scale induction motors are $p = 1, 2, 3$ [27]. Therefore, it seems that the DPNV winding approach is a good match when bearingless motors with $p = 1$ or $p = 2$ are desired. However, from last section, in order to use the parallel PS rotor (that has shorter axial length), the induction motor should have $p_s \geq 2$. In order to use DPNV winding and parallel PS rotor for a 3 phase bearingless induction machine, the only working option therefore becomes $p = 1$, $p_s = 2$, if a symmetric stator winding is highly desired. According to machine design textbook [27], a $p = 1$ induction motor design has large stator and rotor yoke depth, leading to designs with lower torque densities compared to other $p \neq 1$ motors. Torque density matters, for example, when developing bearingless induction machines for mobile applications (i.e. aviation).

This paper is interested in developing $p = 2, 3$ motors using both the DPNV winding and the parallel PS rotor. In [2], it has been reported that the DPNV winding can use less than 2.5% of rated current to support the rotor weight and that a $p = 1, 2$ bearingless induction motor using an isolated PS rotor and DPNV winding has potential to meet the requirements for industrial applications. This paper shows that the DPNV winding can also be used to improve the performance of $p \geq 2$, $p_s \geq 2$ bearingless induction motors with parallel PS rotors.

This section will now present two example asymmetric DPNV winding designs with $p = 2$, $p_s = 3$ that violate the symmetry condition of DPNV windings for symmetric suspension MMF [26, Table III], because p_s is not co-prime with $m = 3$ phases.

3.1 Example Design of an Asymmetric DPNV Winding

The DPNV design process explained in [26, 28] is used to design a stator winding with $Q_s = 18$ slots, $p = 2$ pole-pairs. The star of slots at torque frequency is shown in Figure 3a with a slot angle $\alpha_p = 40^{\text{e}}$. From Figure 3a, phasors belonging to zone +u and zone −u are assigned to phase U, and the phasors in zone -u suggest the corresponding conductors (i.e., $5, 6, 14, 15$) should be connected in reverse to the conductors corresponding to zone +u (i.e., $1, 10$).

For the stator winding in Figure 3a, it is feasible to choose $p_s = 1$ or $p_s = 3$. Since we are interested in using parallel PS rotor, we must select $p_s = 3$. Recall that $p_s = 3 = m$ violates a symmetry condition in [26, Table III], indicating that the suspension MMF will be assymetric. In order to allow the same winding in Figure 3a to produce a suspension field of pole pair number $p_s = 3$ that is different from p, we draw another star of slots at the suspension frequency with $\alpha_{ps} = p_s 360°/Q_s = 60^{\text{e}}$ for each phase, as shown in Figure 3b. The negative signs before phasor numbers account for the connection directions imposed in Figure 3a. To allocate suspension groups, the 360^{e} space is divided into two 180^{e} bands, and phase U phasors in the gray-colored 180^{e} band (i.e., $-6, 10, -14$) will be assigned to group a/c, while the rest (i.e., $1, -5, -15$) are

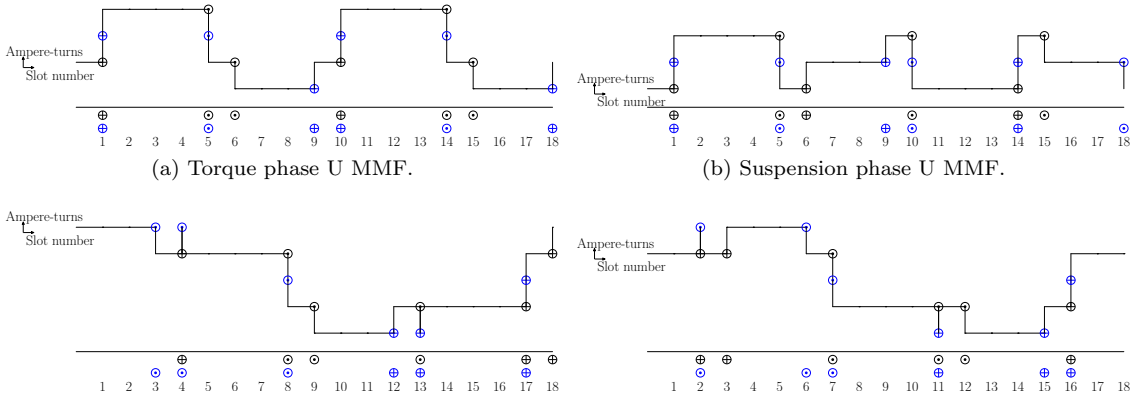

(a) Torque phase U MMF.

(b) Suspension phase U MMF.

(c) Suspension phase V MMF.

(d) Suspension phase W MMF.

Figure 4: MMF waveform of a DPNV winding with $Q_s = 18,\ p = 2,\ p_s = 3,\ y = 4$.

assigned to group b/d. The group name definition is consistent with [26, 28].

3.1.1 Torque MMF Waveform

The example design's torque magnetomotive force (MMF) waveform of phase U is shown in Figure 4a. The torque winding factors, $k_{Tw}(h)$, when the coil pitch y is selected to be 4 slots, are shown in Table 1. The torque winding factor is $k_{Tw}(p) = 0.945$.

3.1.2 Suspension MMF Waveform

The resulting suspension MMF waveforms of phase U, V, and W are shown in Figure 4b-4d and are clearly asymmetric between phases. The MMF of phase U is observed to have a shape that is different from phases V and W; further, the MMF waveform of phase W can be obtained by mirroring about a vertical axis and shifting the MMF waveform of phase V. The suspension winding factors, $k_{Sw}(h)$, are shown in Table 1. Interestingly, it is found that the three phases have the same $k_{Sw}(p_s)$ values of 0.577 for the working harmonic of the suspension field ($h = p_s$). However, the shape asymmetry observed in the MMF waveforms does cause unequal $k_{Sw}(h)$ among 3 phases for the sub-harmonics ($h = 1$) and higher-order harmonics ($h > 3$). The suspension sub-harmonic field has a pole-pair number that differs from p by ± 1, and by interacting with the torque field, it will produce a suspension force.

A second example design for this pole combination is studied in this paper ($p = 2, p_s = 3, Q_s = 24, y = 5$); its winding factors are listed in Table 2. Again, identical $k_{Sw}(p_s)$ is observed for all three phases. One might be tempted to conclude that, for these two particular $p = 2, p_s = 3$ winding designs, the shape asymmetry in the MMF waveform does not incur any problem if we neglect harmonics. Unfortunately, this is not true, as we have only studied the *amplitude asymmetry*, and have not studied the *phase-shift asymmetry*. Different asymmetries are discussed later, in Section 4.

4 Asymmetries in Suspension MMF Waveform

This section investigates the types of asymmetry that arise from violating the DPNV winding symmetry requirement that both p and p_s are co-prime with m listed in [26, Table III]. We care about this because in a previous optimization study [22], the DPNV winding based optimal motor designs with either $p = 3$ or $p_s = 3$ have resulted in significantly shorter rotor axial length, showing the potential to further improve the rotor dynamics for high speed applications.

Table 1: Winding Factors for DPNV winding with $p = 2, p_s = 3, Q_s = 18, y = 4$.

Order h	1	p=2	p_s=3‡	4	5	6	7
$k_{Tw}(h)^*$	-	0.945	-	0.061	-	-0.577	-
$k_{Sw,U}(h)^\dagger$	0.140	-	0.577	-	-0.061	-	-0.945
$k_{Sw,V}(h)$	0.473	-	0.577	-	-0.186	-	-0.398
$k_{Sw,W}(h)$	0.473	-	0.577	-	-0.186	-	-0.398

*$k_{Tw}(h)$ is the torque winding factor for all phases for harmonic order h.
†$k_{Sw,U}(h)$ is the suspension winding factor for phase U for harmonic order h.
‡The phase angles of $\bar{\boldsymbol{k}}_{Sw}(3)$ of the three phases are 0, 120, 240 [elec. deg].

This section is going to use complex winding factors to study asymmetry. The calculated complex number winding factor will allow us to gain insight into two types of asymmetries observed in the winding—whether it is a *phase shift asymmetry*, where the angle between phases are not 120 elec. deg, or whether it is an *amplitude asymmetry*, where not all phases produce the same magnitude of MMF.

4.1 Complex Winding Factor Calculation

This section now introduces a complex winding factor calculation that will be used in later parts of the paper for analysis of winding asymmetry.

The pitch factor for harmonic order $h = vp$ is traditionally computed as

$$k_p(vp) = \sin\left(vp\frac{\gamma}{2}\right) \tag{2}$$

where γ is the coil span in [mech. rad], and $\gamma \in (0, 2\pi)$. Only certain values of γ are allowable, based on the number of stator slots, to make the coil pitch $y = p\gamma/\alpha_u$ an integer, where $\alpha_u = p\frac{2\pi}{Q_s}$ [elec. rad] is the slot angle in star of slots.

This paper only considers the case of a double layer winding where each phasor in the star of slots corresponds to a coil. The location of the coil can then be represented by the phasor number; we can calculate a complex pitch factor for the coil of phasor number $i \in [1, Q_s]$ as

$$\bar{\boldsymbol{k}}_{p,i}(vp) = \sin\left(vp\frac{\alpha_u}{2p}y\right) \mathrm{e}^{j\left[\frac{\pi}{2} - vp\left(\frac{\alpha_u}{2p}(2i+y)\right)\right]} \tag{3}$$

which is a function of the harmonic order $h = vp$ and the winding parameters Q_s, y, p. This definition of pitch factor has the same magnitude as (2), but has an angle indicating the location of the coil. The coil index i for the double layer winding is exactly the phasor number i in the star of slots (see e.g., Figure 3).

The final winding factor takes the winding distribution into account by calculating the "vector average" of the pitch factors of all coils in one phase. For phase U,

$$\bar{\boldsymbol{k}}_{w,U}(vp) \triangleq k_{w,U}(vp)\angle\alpha_{w,U}(vp) = \frac{1}{N_{\mathcal{U}}}\sum_{i\in\mathcal{U}}\bar{\boldsymbol{k}}_{p,i}(vp) \tag{4}$$

where $\mathcal{U}$ is the set of coil indices of phase U, and $N_{\mathcal{U}}$ is the number of coils of phase U. For double layer winding, since each phasor in star of slots corresponds to a coil, we have $\mathcal{U} = \{i \in \mathbb{N} \,|\, \text{star of slots phasor numbers of phase U}\}$, and the set $\mathcal{U}$ will have $N_{\mathcal{U}} = \frac{Q_s}{m}$ elements. For example, Figure 3 gives $\mathcal{U} = \{i \in \mathbb{N} \,|\, 1, 5, 6, 10, 14, 15\}$.

The phase winding MMF can be determined from the winding factor. Here, the vp-th harmonic is expressed for phase U, $\Theta_{U,v}(\alpha)$, as a function of the air gap location α:

$$\Theta_{U,v}(\alpha) = N_{\mathcal{U}}k_{w,U}(vp)\left[\frac{4}{\pi}\frac{\Theta_\pi}{vp}\cos\left(vp\alpha + \alpha_{w,U}(vp) - \frac{\pi}{2}\right)\right] \tag{5}$$

Table 2: Winding Factors for DPNV Winding with $p = 2, p_s = 3, Q_s = 24, y = 5$.

Order h	1	$p = 2$	$p_s = 3^*$	4	5	6	7
$k_{Tw}(n)$	-	0.933	-	-	-	-0.500	-
$k_{Sw,U}(n)$	0.427	-	0.604	-	-0.073	-	-0.427
$k_{Sw,V}(n)$	0.427	-	0.604	-	-0.073	-	-0.427
$k_{Sw,W}(n)$	0.262	-	0.604	-	-0.012	-	-0.695

*The phase angles of $\bar{\boldsymbol{k}}_{Sw}(3)$ of the three phases are 0, 90, 225 [elec. deg].

where $\Theta_\pi = \frac{1}{2} z_Q I_U$ with z_Q the conductor number in a slot and I_U the conductor current. If we calculate the winding factor of each phase, we know the amplitude of the MMF of each phase and that phase's separation from the other phases. In other words, to determine amplitude/phase asymmetry, all we need to do is to calculate the winding factors for all phases.

4.2 Phase-shift Asymmetry

The complex winding factor (4) is useful to determine if there exists *phase-shift asymmetry* in the suspension winding factors among the three phases. For a symmetric three phase winding, the working harmonic's winding factor angle referred to phase U should be a multiple of 120^e,

$$\begin{aligned} \alpha_{w,U} - \alpha_{w,U} &= 0^\text{e} \\ \alpha_{w,V} - \alpha_{w,U} &= 120^\text{e} \\ \alpha_{w,W} - \alpha_{w,U} &= 240^\text{e} \end{aligned} \tag{6}$$

where $\alpha_{w,X},\ X = U, V, W$ is the winding factor angle defined in (4).

In Table 2, when $h = p_s = 3$, the winding factor angles are $0^\text{e},\ 90^\text{e},\ 225^\text{e}$, which means there exists phase-shift asymmetry, though there is no amplitude asymmetry.

In Table 1, when $h = p_s = 3$, the winding factor angles are $0^\text{e},\ 120^\text{e},\ 240^\text{e}$, which means there is no phase-shift asymmetry. It is surprising to find that there is neither amplitude asymmetry nor phase-shift asymmetry at the working harmonic $h = p_s = 3$ for a symmetry condition violating DPNV winding (recall that there is amplitude asymmetry in the subharmonics).

4.3 Amplitude Asymmetry

Symmetric three phase winding will have the same winding factor amplitude for each phase. For example, the two windings shown in Table 2 and Table 1 do not experience amplitude asymmetry for the working harmonic $h = p_s$, though there are amplitude asymmetry in other harmonics $h \neq p_s$.

We now introduce a third example winding with $p = 3, p_s = 4, Q_s = 36, y = 5$ in Table 3. This winding does exhibit amplitude asymmetry for harmonic $h = p_s$[1].

4.4 Discussion

If a symmetric suspension MMF profile for $p=3$ or $p_s=3$ motors is desired, there are at least two alternatives, 1) use a separated winding approach; 2) use a non-three-phase DPNV winding. However, as previously noted, the separated winding makes inefficient use of the slot area, significantly decreasing the machine's torque density, and the non-three-phase DPNV winding loses the merit/convenience of compatibility with existing commercial three phase motor drives.

Instead of pursuing these alternatives, this paper studies the performance impact of designing with an assymetric DPNV winding. Hints that this may be feasible can be found in Table 1, where the DPNV winding ($p = 2,\ p_s = 3,\ Q_s = 18$) has no asymmetry if harmonics are neglected.

[1] With less stator slots, the winding of $p = 3, p_s = 4, Q_s = 18, y = 3$ has no amplitude asymmetry for having the same $k_{Sw}(p_s) = 0.577$ for three phases, but phase-shift asymmetry still exists.

Table 3: Winding Factors for Design No. 7 ($p = 3, p_s = 4, Q_s = 36, y = 5$).

Order h	1	2	$p = 3$	$p_s = 4^*$	5	6
$k_{Tw}(h)$	-	-	0.933	-	-	-
$k_{Sw,U}(h)$	-	0.391	-	0.647	-	0.083
$k_{Sw,V}(h)$	-	0.503	-	0.617	-	0.144
$k_{Sw,W}(h)$	-	0.391	-	0.647	-	0.083

*The phase angles of $\bar{\boldsymbol{k}}_{Sw}(4)$ of the three phases are 0, 110, -140 [elec. deg].

5 Suspension Harmonics of DPNV Winding

Sub-harmonics are often seen in a fractional slot winding. Even if the induction motor uses integral slot torque winding, the suspension slot per pole per phase $q_s = \frac{Q_s}{2mp_s}$ can still be a fractional number. In this paper, the sub-harmonics are examined by calculating the winding factor for arbitrary harmonic order $h = vp$ or $h = vp_s$ using (4). Sub-harmonics are not caused by violation of symmetry condition, and are common phenomena observed in DPNV winding suspension winding factors when $p_s > 2$.

5.1 Attenuation of Unmodeled Suspension Force

The sub-harmonics of the suspension field can interact with the torque field to generate unmodeled suspension force as long as the rotor uses soft magnetic materials (steels). Note sometimes higher harmonics could also contribute to the unmodeled suspension force, e.g, the harmonic of order $h = 4$ of the $p = 3, p_s = 2$ winding. By "unmodeled", we mean this force contribution is not intentionally utilized during bearingless motor design phase, so it is desired to reduce this unmodeled suspension force.

Recall that with a conventional squirrel cage, the suspension force is attenuated as the stator current frequency increases [15]. If a parallel PS rotor is used, the sub-harmonics will also induce rotor currents, since the rotor was not designed to reject the number of poles of the sub-harmonic field. The induced sub-harmonic rotor currents can interact with the sub-harmonic suspension field to create asynchronous torque, which is undesired but is frequently insignificant. These rotor currents may actually partially cancel out the sub-harmonic suspension field and thereby attenuate the unmodeled suspension force.

It is not straightforward to determine whether the sub-harmonics are detrimental or beneficial to the suspension force performance. To answer this question, it is necessary to learn the rotating direction of the harmonic field. If the sub-harmonic field rotates in the same direction as the torque field, it will produce constant force; while if it is reversed, it causes a force disturbance [29, Sec. II-B2].

5.2 Asymmetric Sub-harmonics

For all windings investigated in this paper, when p or p_s is not co-prime with the phase number $m = 3$, if the sub-harmonics exist, the suspension winding factors of the sub-harmonics are asymmetric in both amplitude and phase-shift. Since the sub-harmonics of order $h = p \pm 1$ will contribute to the radial force, we expect this sub-harmonic asymmetry to cause problems. In other words, we expect that the "promising" DPNV winding from Table 1, will still show some undesired behavior because of asymmetric sub-harmonics. This undesired behavior will be revealed later in Section 6.3.

6 FEA Results in Polar Plots

The purpose of this section is to determine whether MMF asymmetries and sub-harmonics create force performance issues for bearingless induction motors.

Table 4: List of Selected Optimal Designs from [22] for 50 kW and 30,000 r/min Application.

Design No. & Name	q	q_s	Q'_r	k_{Tw}	$\bar{\boldsymbol{k}}_{Sw,U}$, $\bar{\boldsymbol{k}}_{Sw,V}$, $\bar{\boldsymbol{k}}_{Sw,W}$	L_{stk},	L_{ew},	$L_{\text{stk}}+L_{\text{ew}}$ [mm]
1. p1p$_s$2Q$_r$14Q$_s$24y9	4	2	2	0.885	$0.592\angle 0^e$, $0.592\angle 120^e$, $0.592\angle 240^e$	**91**	30	**121**
2. p2p$_s$3Q$_r$30Q$_s$18y4	$\frac{3}{2}$	1	3	0.945	$0.577\angle 0^e$, $0.577\angle 120^e$, $0.577\angle 240^e$	110	32	142
3. p2p$_s$3Q$_r$18Q$_s$24y5	2	$\frac{4}{3}$	3	0.933	$0.604\angle 0^e$, $0.604\angle 90^e$, $0.604\angle 225^e$	105	21	126
4. p3p$_s$2Q$_r$20Q$_s$36y5	2	3	2	0.933	$0.503\angle 0^e$, $0.480\angle 130^e$, $0.503\angle 260^e$	98	33	131
5. p3p$_s$4Q$_r$20Q$_s$36y5	2	$\frac{3}{2}$	4	0.933	$0.647\angle 0^e$, $0.617\angle 110^e$, $0.647\angle 220^e$	110	**16**	126
6. p4p$_s$5Q$_r$20Q$_s$24y3	1	$\frac{4}{5}$	5	1.000	$0.604\angle 0^e$, $0.604\angle 120^e$, $0.604\angle 240^e$	-	-	-

Note: L_{stk}, L_{ew} is the axial length of the rotor lamination stack, end-ring region.

Note: q is slot per phase per torque pole, and q_s is slot per phase per suspension pole.

6.1 Optimal Designs Adapted from a Previous Research

Table 4 lists the six designs to be studied in this paper. The first 5 designs in Table 4 are the selected optimal designs from [22], meaning that this paper is an extension of the previous research in studying optimized bearingless induction motor designs for the rating of 50 kW and 30,000 r/min. As an example of a winding that has sub-harmonics but no asymmetry, a sixth design of $p = 4, p_s = 5$ is added as design 6. Note that design 6 is not optimized.

In Table 4, the slot per phase per torque pole q, the slot per phase per suspension pole q_s, the cage number N_c, torque winding factor, complex number suspension winding factors and rotor axial length are summarized. As per [22], it should be emphasized that the high p_s design, i.e., design 5, with $Q'_r = 4, Q_r = 20$ has significantly shorter eng-ring region length L_{ew}, as compared with design 1 having even less rotor slots of $Q_r = 14$.

As a companion table of Table 4, Table 5 summarizes the asymmetries and harmonics properties of each design, followed by performance results that are explained in the next subsection.

6.2 Simulation Approach and Analyzing Tool

2D transient finite element analysis (FEA) using JMAG Designer is conducted for evaluating the steady state force vectors at rated operating conditions of 50 kW and 30,000 r/min. In FEA, the motor and suspension terminals of the stator DPNV winding are both excited with sinusoidal currents at the same frequency, and there is a *phase delay*, ϕ_{sus}, between the motor currents and suspension currents. Rated coil group current is flowing with 2.5% allocated for suspension and 97.5% allocated for torque.

We use polar plots to visualize how the force vectors vary as a function of $\phi_{\text{sus}} \in [0, 360]$ [elec. deg]. The steady state force vectors will rotate along the air gap when ϕ_{sus} changes. In a first series of plots (Figure 5), we depict the average force vector amplitude against the average force vector angle as a "force polar plot" (FPP). In a second series of plots (Figure 6), we depict the force error angle against the average force vector angle as a "E_a polar plot" (E_a-PP). Here the force error angle E_a is defined as the maximum angle deviation of the force vector from the average force vector at steady state over one fundamental period. It is worth mentioning that the steady state of a design with sub-harmonics needs to be evaluated for longer time, which is related to the period of the sub-harmonics, as reported in [28].

6.3 Force Polar Plot (FPP)

A circular FPP is generally desired, but elliptical FPP can result for an asymmetric DPNV winding. For elliptic FPP, the force rating of the machine must be de-rated to correspond to the minimum radius of the ellipse.

The force polar plots of the six designs listed in Table 4 are shown in Figure 5. The phase angle of the suspension currents, ϕ_{sus}, that corresponds to the minimum or maximum of the elliptical FPP is indicated using a red or blue arrow.

Table 5: Asymmetries, Harmonics and Performance Measure of the Designs from Table 4.

Design No.	1	2	3	4	5	6
Harmonics at $h = p \pm 1$	-*	✓†	✓	✓	✓	✓
Amplitude asymmetry in working harmonics $h = p_s$	-	-	-	✓	✓	-
Phase-shift asymmetry in working harmonics $h = p_s$	-	-	✓	✓	✓	-
Asymmetry in harmonics $h = p \pm 1$	-	✓	✓	✓	✓	-
Elliptical force polar plot?	No	Yes	Yes	Yes	Yes	No
Maximal force variation in FPP, ΔF [N]	0.06	5.6	9.4	27.5	5.3	0.27
Maximal E_a variation in E_a-PP, ΔE_a [mech. deg]	**0.8**	**2.1**	5.2	9.0	**2.3**	7.4
Acceptable Design?	**Yes**	**Yes**	No	No	**Yes**	No

*Check mark "✓" means the description applies.
†Dash "-" means the description does not apply.

Based on Figure 5, the following observations can be made.

1. *Windings that have no asymmetry and no sub-harmonics have circular FPP.* E.g., the $p = 1,\ p_s = 2$ winding in Figure 5a.

2. *Symmetric windings that have sub-harmonics have circular FPP.* E.g., the $p = 4, p_s = 5$ winding in Figure 5f.

3. *Windings that have asymmetry in sub-harmonics and have no asymmetry in working-harmonics have elliptical FPP.* E.g., the $p = 2, p_s = 3, Q_s = 18$ winding in Figure 5b.

4. *Windings that have asymmetry in working-harmonics have elliptical FPP.* E.g., Figure 5c–5e.

This shows that even asymmetry in the sub-harmonics (when the working harmonics are symmetric) can cause elliptical FPP. This indirectly verifies the fact that sub-harmonics do contribute to bearingless motor's suspension force capability. In conclusion, the elliptical FPP is due to i) the (amplitude and phase-shift) asymmetries in suspension winding factor at $h = p_s = p \pm 1$, and ii) the asymmetric harmonics that satisfy $h = p \pm 1$. The above observations are compactly summarized as Table 5.

All windings that violate the DPNV winding symmetry condition by having either $p = 3$ or $p_s = 3$ show elliptical FPP. As a performance measure, let ΔF designate the difference between maximal force and minimal force of an FPP, i.e., the length difference between the blue and red arrows in Figure 5. The ΔF values for the six designs are listed in Table 5. It is desired to have zero or low ΔF. Symmetric windings have close to zero ΔF values, e.g., design 1 and 6. For asymmetric windings, design 3 and 4 show large ΔF values, but we do observe low ΔF values in design 2 that has no asymmetry in working-harmonics and design 5 that has asymmetry in both working and sub-harmonics. This provides evidence that a DPNV winding with asymmetry in both the working and subharmonics can yield acceptable force performance.

6.4 Force Error Angle Polar Plot

Force error angle E_a as a function of suspension current angle ϕ_{sus} is sketched as polar plot in Figure 6 for all six designs. Again, only the first five designs are optimal designs selected from the Pareto front in [22]. From Figure 6, it is observed that E_a is generally a function of ϕ_{sus}, and the E_a polar plot (E_a-PP) exhibits different trajectory patterns for different motor designs, and the trajectory patten is mirrored about the origin.

All E_a-PPs are drawn at the same scale to ease visual comparison of the variation in E_a values when ϕ_{sus} changes. As a performance measure, the maximal variation in E_a values in

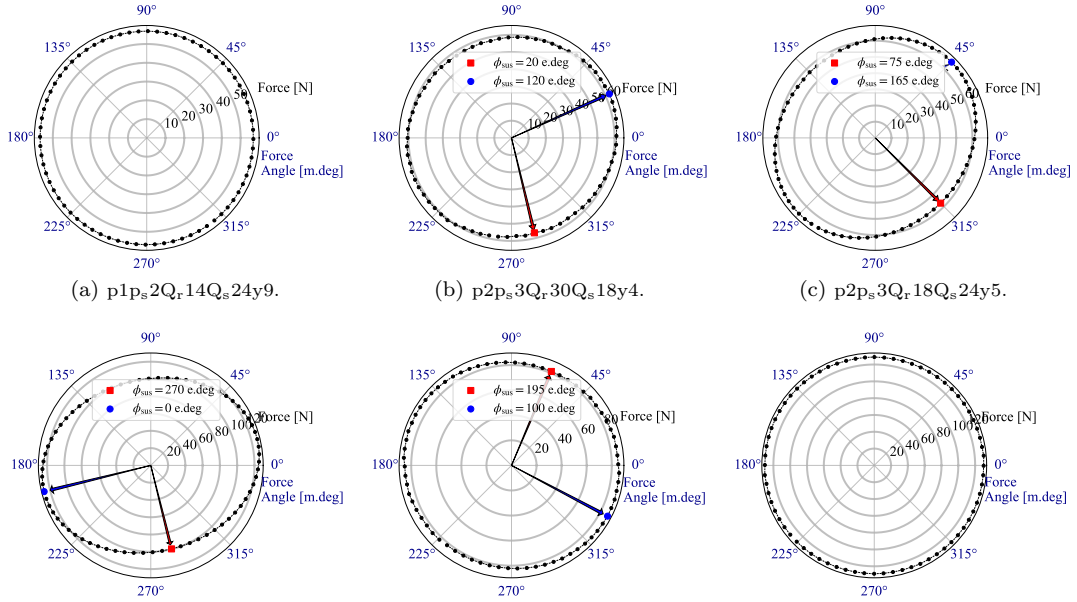

(a) p1p$_s$2Q$_r$14Q$_s$24y9. (b) p2p$_s$3Q$_r$30Q$_s$18y4. (c) p2p$_s$3Q$_r$18Q$_s$24y5.

(d) p3p$_s$2Q$_r$20Q$_s$36y5. (e) p3p$_s$4Q$_r$20Q$_s$36y5. (f) p4p$_s$5Q$_r$20Q$_s$24y3.

Figure 5: Force polar plots of the designs listed in Table 4.

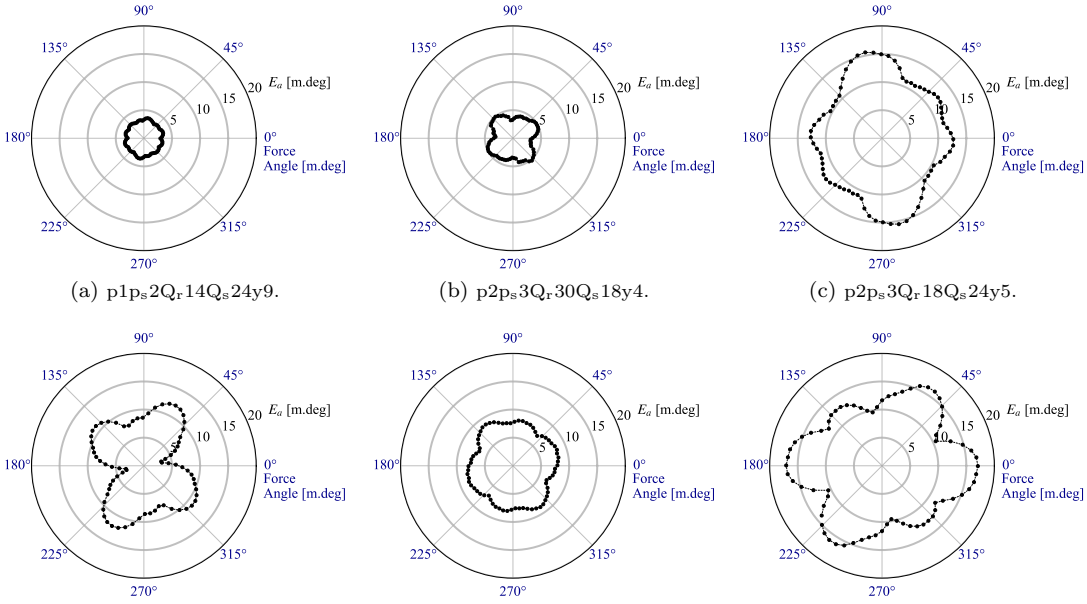

(a) p1p$_s$2Q$_r$14Q$_s$24y9. (b) p2p$_s$3Q$_r$30Q$_s$18y4. (c) p2p$_s$3Q$_r$18Q$_s$24y5.

(d) p3p$_s$2Q$_r$20Q$_s$36y5. (e) p3p$_s$4Q$_r$20Q$_s$36y5. (f) p4p$_s$5Q$_r$20Q$_s$24y3.

Figure 6: Force error angle E_a polar plots of the designs listed in Table 4.

an E_a-PP is denoted as ΔE_a and is summarized in Table 5 for all six designs. We suggest to one use a design that has low ΔE_a, e.g., design 1, 2, and 5.

In conclusion, there is no clear correlation between the shape of FPP and the shape of E_a-PP, and the asymmetric DPNV winding can result in acceptable bearingless induction motor design, in a sense that its ΔF and ΔE_a are both reasonably small, e.g., design 2 and design 5.

7 Conclusion

The DPNV winding and parallel PS rotor are two recent technologies that can be used to create industrial scale, power dense bearingless induction motors. Preliminary optimization results indicate that by using these two technologies, bearingless induction machines can meet the requirements of industrial compressor systems. However, two desired machine pole combinations result in asymmetric stator windings and require further investigation to determine if acceptable machine performance can be achieved. This paper finds that the asymmetry of the DPNV winding can be studied by using complex winding factors of each winding phase. Based on transient FEA results, this paper uses a force polar plot to visually study the steady state force vector behavior of five selected optimal designs. Observations are drawn on the influence of asymmetries combined with the DPNV winding's inherent sub-harmonic fields. By using FPP, it is found that MMF asymmetry causes an elliptical force capability that reduces the machine's force rating. The level of force reduction varied between machines from being negligible to being a significant concern. From an E_a-PP, it is revealed that force error angle of a bearingless induction motor is dependent on the suspension current phase angle. This latter finding imposes a challenge to accurately evaluate the force vector error of a bearingless motor design. Future research is needed to take the suspension current phase angle into account in order to accurately model bearingless motors and avoid under-calculating the force error angle performance metric.

Together, the findings from this paper provide evidence that asymmetric DPNV windings can be used with the parallel PS rotor to create a high performance bearingless induction machine. The nuances in performance between designs imply that careful attention must be paid in the design and optimization process of both asymmetric and symmetric designs to ensure accurate performance calculations are made.

References

[1] A. Chiba, T. Fukao, O. Ichikawa, M. Oshima, M. Takemoto, and D. G. Dorrell, *Magnetic bearings and bearingless drives*. Elsevier, 2005.

[2] J. Chen, Y. Fujii, M. W. Johnson, A. Farhan, and E. L. Severson, "Optimal design of the bearingless induction motor," *IEEE Transactions on Industry Applications*, vol. 57, no. 2, pp. 1375–1388, 2021.

[3] J. Chen, J. Zhu, and E. L. Severson, "Review of bearingless motor technology for significant power applications," *IEEE Transactions on Industry Applications*, vol. 56, no. 2, pp. 1377–1388, 2020.

[4] M. Kang, J. Huang, J.-q. Yang, and H.-b. Jiang, "Analysis and experiment of a 6-phase bearingless induction motor," in *2008 International Conference on Electrical Machines and Systems*. IEEE, 2008, pp. 990–994.

[5] M. T. Bartholet, T. Nussbaumer, S. Silber, and J. W. Kolar, "Comparative evaluation of polyphase bearingless slice motors for fluid-handling applications," *IEEE Transactions on Industry Applications*, vol. 45, no. 5, pp. 1821–1830, 2009.

[6] W. Khoo, "Bridge configured winding for polyphase self-bearing machines," *IEEE Trans on Magnetics*, vol. 41, no. 4, pp. 1289–1295, 2005.

[7] R. Oishi, S. Horima, H. Sugimoto, and A. Chiba, "A novel parallel motor winding structure for bearingless motors," *IEEE Transactions on Magnetics*, vol. 49, no. 5, pp. 2287–2290, May 2013.

[8] G. Valente, L. Papini, A. Formentini, C. Gerada, and P. Zanchetta, "Radial force control of multisector permanent-magnet machines for vibration suppression," *IEEE Transactions on Industrial Electronics*, vol. 65, no. 7, pp. 5395–5405, 2017.

[9] S. Kobayashi, M. Ooshima, and M. N. Uddin, "A radial position control method of bearingless motor based on d-q-axis current control," *IEEE Transactions on Industry Applications*, vol. 49, no. 4, pp. 1827–1835, 2013.

[10] A. Chiba, K. Sotome, Y. Iiyama, and M. A. Rahman, "A novel middle-point-current-injection-type bearingless pm synchronous motor for vibration suppression," *IEEE Transactions on Industry Applications*, vol. 47, no. 4, pp. 1700–1706, July 2011.

[11] A. Khamitov, W. Gruber, G. Bramerdorfer, and E. L. Severson, "Comparison of combined winding strategies for radial non-salient bearingless machines," *IEEE Transactions on Industry Applications*, 2021.

[12] A. Chiba, D. Power, and M. Rahman, "Characteristics of a bearingless induction motor," *IEEE Transactions on Magnetics*, vol. 27, no. 6, pp. 5199–5201, 1991.

[13] A. Salazar and R. Stephan, "A bearingless method for induction machines," *IEEE Trans on Magnetics*, vol. 29, no. 6, pp. 2965–2967, 1993.

[14] T. Katou, A. Chiba, and T. Fukao, "Magnetic suspension force in an induction bearingless motor with a squirrel cage rotor," *Electrical Engineering in Japan*, vol. 159, no. 3, pp. 77–87, 2007.

[15] J. Chen and E. L. Severson, "Design and modeling of the bearingless induction motor," in *2019 IEEE International Electric Machines Drives Conference (IEMDC)*, May 2019, pp. 343–350.

[16] C. Redemann, P. Meuter, A. Ramella, and T. Gempp, "30kw bearingless canned motor pump on the test bed," in *7th International Symp. on Magnetic Bearings, August 2000, ETH Zurich*, 2000.

[17] H. J. Herbein, *Rotating Machinery*. Rinehart Press, 1971.

[18] J. M. S. Ferreira, M. Zucca, A. O. Salazar, and L. Donadio, "Analysis of a bearingless machine with divided windings," *IEEE Transactions on Magnetics*, vol. 41, no. 10, pp. 3931–3933, Oct 2005.

[19] A. Chiba, "Transfer characteristics of radial force of induction-type bearingless motors with four-pole rotor circuits," in *The 5th International Symposium on Magnetic Bearings (ISMB5)*, Aug 1996, pp. 319–325.

[20] A. Chiba and T. Fukao, "Optimal design of rotor circuits in induction type bearingless motors," in *1998 IEEE International Magnetics Conference (INTERMAG)*, Jan 1998, pp. 225–225.

[21] A. Chiba and J. Asama, "Influence of rotor skew in induction type bearingless motor," *IEEE Transactions on Magnetics*, vol. 48, no. 11, pp. 4646–4649, 2012.

[22] J. Chen, M. Johnson, A. Farhan, Y. Fujii, and E. L. Severson, "Reduced axial length pole-specific rotor forbearingless induction machines," *IEEE Transactions on Energy Conversion*, 2021.

[23] A. Chiba and J. Asama, "Influence of rotor skew in induction type bearingless motor," *IEEE Transactions on Magnetics*, vol. 48, no. 11, pp. 4646–4649, 2012.

[24] A. Chiba and J. A. Santisteban, "A pwm harmonics elimination method in simultaneous estimation of magnetic field and displacements in bearingless induction motors," *IEEE Transactions on Industry Applications*, vol. 48, no. 1, pp. 124–131, Jan 2012.

[25] D. Dietz and A. Binder, "Design guidelines and scaling effects for bearingless pm synchronous machines accounting for eddy current reaction field," *IEEE Transactions on Industry Applications*, 2021.

[26] E. L. Severson, R. Nilssen, T. Undeland, and N. Mohan, "Design of dual purpose no-voltage combined windings for bearingless motors," *IEEE Transactions on Industry Applications*, vol. 53, no. 5, pp. 4368–4379, 2017.

[27] J. Pyrhonen, T. Jokinen, and V. Hrabovcová, *Design of rotating electrical machines*. John Wiley & Sons, 2013.

[28] J. Chen, A. Farhan, M. Johnson, and E. L. Severson, "Design of bearingless permanent magnet motors using no voltage combined windings," *IET Conference Proceedings*, pp. 803–808(5), 2021.

[29] B. Ramadas and E. L. Severson, "Suspension force design guidelines for bearingless permanent magnet machines," in *IEEE Energy Conversion Congress and Exposition (ECCE)*, 2021.